1

Coupled H and Nb-, Cr- and V trace element behavior in synthetic rutile at 600°C, 400 MPa and possible geological application

1 revised version of ms 4183

Friedrich Lucassen [1,2]*, Monika Koch-Müller[2], Michail Taran[3], Gerhard Franz[1]

(1)Technische Universität Berlin, Fachgebiet Petrologie. Berlin, Germany

(2)Deutsches Geoforschungszentrum; Potsdam, Germany

(3)National Academy of Sciences of Ukraine; Kyiv, Ukraine

*now at Fachgebiet Isotopengeochemie, FB 5 Geowissenschaften, Universität Bremen

Abstract

We performed hydration experiments of pure and Nb-, Cr-, and V-doped synthetic dry (H_2O <3ppm) single rutile crystals. They were equilibrated with pure H_2O in hydrothermal experiments at constant conditions of 600 °C, 400 MPa and fO_2 near the Ni–NiO buffer, run time between ~25 min and 14 days. Slabs cut parallel to (110) of the reacted single crystals (1 to 2 mm^3) were analyzed for H^+ by FTIR. Hydration occurs almost spontaneously and the H_2O-equivalent is uniformly distributed in the samples, but depends extremely on trace element contents. In pure rutile, the average H_2O-content is 314±50 ppm, the saturation level at these conditions. Rutile doped with 500 ppm Nb has a lower average H_2O content of ~235 ppm, rutile with 2000 ppm Cr has ~900 ppm H_2O, and rutile with 2000 ppm V does not incorporate H_2O. During stepwise heating at atmospheric pressure of a reacted Nb-doped rutile, H^+ is quickly released between 450 and 550 °C. UV-VIS spectra of unreacted colorless and reacted deep blue pure rutile show the rutile-characteristic sharp absorption edge in the UV spectra. The reacted rutile has a broad absorption band at 6500 cm^{-1} wavenumber attributed to intervalence charge transfer transition $Ti^{3+} + Ti^{4+} \rightarrow Ti^{4+} + Ti^{3+}$. The reduction of Ti^{4+} to Ti^{3+} is charge balanced by the incorporation of H^+. The Nb-doped rutile changed its color from light greenish-blue (untreated) to deep blue. In the untreated Nb rutile the UV-VIS absorption band at 6500 cm^{-1} indicates that Nb^{5+} is charge balanced by Ti^{3+}. In the reacted Nb-rutile the absorption band is more intense, but compared with the pure rutile, H^+ incorporation is lower by the equivalent of Ti^{3+} reduced in the untreated rutile. Reacted Cr-rutile almost retains its brownish-orange color, but the spectrum shows a prominent Ti^{3+}/Ti^{4+} IVCT band at ~ 6400 cm^{-1} with moderate intensity considering the high H_2O contents of ~900 ppm. The high H^+ contents are best explained by the reduction of Cr^{4+} to Cr^{2+}. The UV-VIS spectra of the dark-blue to opaque V-doped rutile show a very strong absorption towards low energies, which is likely caused by

41   reduction of Ti^{4+} to Ti^{3+} for charge balance of V^{5+}. This forms a deep narrow window of

42   transmittance in the range $25,000 – 20,000$ cm^{-1}, which causes the dark-blue color.

43   To explore the possible use of H-in-rutile as a geohygrometer, geothermobarometer and

44   oxybarometer, we measured the H^+ content in a natural rutile crystal from a retrograded eclogite

45   with a zoned trace element (Fe, Nb, and Zr) content. The crystal reveals a slight correlation between

46   the variable H_2O (~200 to 900 ppm) and its trace element concentrations. The observations indicate

47   that the preservation of H^+ contents in this natural rutile is a complicated interplay of diffusive

48   reequlibration of fast H^+, slower Fe and very slow other trace elements. An interpretation of the

49   H_2O contents of the natural crystal in terms of f_{O2} or a_{H2O} is not possible.

50   **Key words:** Experimental petrology, rutile, NAM, UV-VIS spectroscopy

51

52   **Introduction**

53

54   Rutile (TiO_2) is a common accessory mineral in many rocks and an important carrier of trace

55   elements such as Nb, Ta, Zr, V, and Cr especially in metamorphosed mafic rocks at elevated

56   pressures (e.g., Zack et al. 2002; Schmidt et al. 2009). It is also known that this nominally

57   anhydrous mineral can contain up to several 1000 ppm of water, especially in high and ultrahigh

58   pressure rocks (Bell and Rossman 1992; Katayama et al. 2006; Zheng 2009). The incorporation of

59   H^+ into natural rutile from different geological environments has been discussed in terms of H_2O-

60   pressure (e.g., Hammer and Beran 1991) and charge balance considerations, substituting Ti^{4+} by

61   trace elements such as Nb and Cr^{3+} (e.g., Vlassopoulos et al. 1993). The reaction of Ti-reduction

62   and H^+-incorporation can be formulated as

63                    $$Ti^{4+}O_2 + e^- + H^+ = Ti^{3+}OOH.$$

64   The use of H^+ in chemically pure rutile as a geohygrometer, geothermobarometer and oxybarometer

65   was experimentally explored (Vlassopoulos et al. 1993; Colasanti et al. 2011), but the application to

66   geological environments has still to be investigated, because diffusion of H^+ in single crystal rutile

67   is known to be fast (e.g., Johnson et al. 1975).

68   Previous experimental studies of H^+ incorporation in rutile under geologically relevant

69   conditions mainly focused on high pressure and high temperature conditions (*P* up to 50 GPa, T

70   1500 °C; Khomenko et al. 1998; Bromiley et al. 2004; Bromiley and Hilairet 2005). In these

71   experiments, rutile was synthesized from powdered TiO_2 or mixtures with Fe, Nb, Cr oxide

72   powders, and H_2O, i.e. new rutile crystals grew in the presence of hydrogen. Colasanti et al. (2011)

73   used a different method and started from synthetic, chemically pure and dry single crystal rutile and

3

74   investigated the hydration behavior under water saturated conditions in a series of experiments at

75   P_{H2O} of 0.5 and 1.0 GPa and T 500 to 900°C and variable f_{O2}.

76   At near ambient pressure incorporation of hydrogen is known from synthetic single crystal

77   rutile grown by flame fusion (Verneuil method) above 1825 °C (e.g., Soffer, 1961) or from

78   experiments at temperatures up to 800 °C and low P in a controlled H_2O or H_2 gas atmosphere (e.g.

79   Johnson et al. 1973, 1975; Herklotz et al. 2011). Abundant experimental and theoretical work on

80   trace element doped TiO_2 (anatase and rutile) in material sciences focuses on catalytic (e.g. Luo et

81   al. 2012) and conductive (e.g. Di Valentin et al. 2009) properties of this important industrial

82   material (e.g. Fujishima and Honda 1972; Chen and Mao 2007; Zaleska 2008). However synthetic

83   materials mainly include nano-sized powders and thin films or ceramics with high surface/mass

84   ratio, which cannot be compared with rutile as a rock constituent. Only Luo et al. (2012) studied the

85   possible use of natural rutile, annealed under argon, for photocatalytic applications.

86   This study explores H^+ incorporation into ~ 1 to 2 mm^3 large, crystallographically oriented,

87   synthetic pure and Cr-, Nb-, and V- doped rutile of low initial H^+ contents (~ 3 ppm H_2O

88   equivalent) from the geological point of view, following the studies of Vlassopoulos et al. (1993),

89   Bromiley and Hilairet (2005) and Colasanti et al. (2011). We used UV-VIS for the exploration of

90   color changes in the hydration experiment, which gives important information about the valence

91   state of Ti and the trace elements. The large crystals allows measuring the areal distribution of H^+ in

92   the rutile (determined by FTIR, Fourier transform infrared spectroscopy). Physical conditions for

93   the treatment are 600 °C and 400 MPa and thus within the amphibolite facies field, where

94   rehydration of high-grade metamorphic rocks occurs within the crust. We also show data of trace

95   element and H^+ contents of a natural rutile crystal with a cooling history on the geological time

96   scale and discuss the possible geological implications. We will show that substituting elements in

97   rutile strongly influence the amount of H^+, which can be incorporated into rutile. The interaction of

98   variably charged cations, e.g., Nb^{5+} and V^{5+} with Ti^{4+}/Ti^{3+} reduces the amount of Ti^{3+} for charge

99   balance that is not available for the reaction $Ti^{4+}O_2 + e^- + H^+ = Ti^{3+}OOH$, whereas Cr allows the

100   incorporation of additional H^+. Charge transfer reactions are very fast and will not survive

101   geological time scales or at least they record a late stage of the thermal and f_{O2} evolution.

102   Interpretation in terms of changing f_{O2} or H_2O activity is impossible.

103

104   **Experimental setup, methods, and materials**

105

106   Syntheses

4

107   The rutile was grown by the Verneuil method from 99.99% grade TiO_2 using a three-tube

108   flame burner for flame fusion technique, melting point was controlled by differential thermal

109   analysis with an accuracy of ±5°C. It is orientated with one (110) face polished by the manufacturer

110   (SurfaceNet GmbH, Rheine, Germany). Orientation was made by the manufacturer with a

111   digitalized Laue X-ray equipment and checked by us with a polarization microscope, which showed

112   perfect orientation of the slabs with c-axis parallel to the surface. The deviation from the exact

113   orientation did not exceed ~2°. Dopants were added as Fe_2O_3, Cr_2O_3, Nb_2O_5 and V_2O_5 and mixed

114   with the starting TiO_2 powder. The crystals was cut into pieces of ~1 mm edge length (Fig. 1) or 1 x

115   1 x 2 mm perpendicular to (110). Verneuil grown rutile is treated by the manufacturer in oxygen

116   atmosphere at high T and is hence fully oxidized, i.e. the undoped pure rutile is clear and Fe-, Cr-,

117   and Nb-doped species are transparent. In the Fe-doped rutile the Fe content is below the detection

118   limit of the electron microprobe (EMP, see below). The traces of Fe produce its slightly brownish-

119   yellow color. Because we did not observe differences in our experiments with pure and with Fe-

120   doped crystals, both are considered as 'pure'. The other specimens are doped with 500 ppm Nb,

121   2000 ppm Cr, and 2000 ppm V respectively. The color of the Nb-doped rutile is emerald green and

122   that of Cr-doped rutile orange-red, the V-doped rutile is of low transparency. Trace element

123   contents and homogeneity of their distribution were controlled by EMP measurements and by laser

124   ablation (LA-ICP-MS; for the applied technique see Lucassen et al. 2010a, 2011) on selected

125   samples. EMP analyses were made in the wave-length disversive mode with a Cameca SX 100

126   EMP at the Deutsches GeoForschungsZentrum. The raw intensity data were corrected with the

127   'PAP' program (Pouchou and Pichoir 1988). Beam conditions were an accelerating voltage of 15

128   kV, a beam current of 100 nA, a beam size of 1 μm, and counting times of 300 s on the peak.

129   Synthetic standards Cr_2O_3, Nb-metal and Fe_2O_3 were used. Fixed values for the major elements

130   were included in the correction procedure. The detection limit was for 50 μg/g Nb, 40 μg/g for Fe,

131   45 μm/g for Cr. No other elements were detected. The time-resolved LA-ICPMS spectra show no

132   relation of the calculated ^{93}Nb intensities to spot size (60, 44, and 32 μm diameter) or depth (time)

133   and Nb distribution in the rutile is uniform at this scale. In individual EMP analyses with a beam

134   size of 1 to 2 μm and the corresponding excitation volume the Nb contents in the crystals varies

135   between 330 and 620 μg/g, but is more uniform between 460 and 512 μg/g in LA-ICP-MS analyses

136   The average Nb contents of the rutile from EMP (502±68 μg/g, n = 78) and LA-ICP-MS (480±19

137   μg/g, n = 22) are similar. The Cr content is uniform with ~2000 μg/g (EMP average 2016±42 μg/g;

138   n = 30; LA-ICP-MS average 2010±43 μg/g; n = 21). For V, which was not determined, we relied on

139   the nominal amount given by the manufacturer, water contents were determined by us. H_2O

140   equivalent in the untreated pure and Fe-doped rutile is ~3 ppm, determined by FTIR (Fig. 2).

5

141   Polarized Raman spectra of the untreated pure, the Nb-, and Cr-doped rutile are very similar and we

142   conclude that they contain similarly low amount of H^+, whereas no OH signal was found in spectra

143   of the V doped rutile.

144   The rutile crystals (Fig. 1) were loaded together with pure H_2O into gold capsules of ~25

145   mm length, 3 mm diameter and wall thickness of 0.15 mm. The capsules were sealed by arc

146   welding. All experiments were conducted at Technische Universität Berlin in cold seal autoclaves at

147   600 °C, and 400 MPa, pressurized by water. Temperature and pressure reading is within ± 10 °C

148   and ± 10 MPa. The f_{O2} is close to the nickel-nickeloxide (NNO) buffer by the Ni-bearing material of

149   the autoclave and filler rods. Samples were first pressurized and then isobarically heated to 600 °C

150   within ~20 minutes. During isobaric cooling of the autoclaves in an air-stream T below 400 °C was

151   reached within one minute and ambient temperature in < than five minutes. The crystals were

152   checked under the scanning electron microscope (SEM) for possible changes by dissolution on the

153   surface, which was not observed on a scale of ≤1 µm. In a companion study (about the trace

154   element content in synthetic titanite grown from identical crystals) we used the JEOL JXA-8500F

155   hyperprobe, which has a resolution of ~100 nm and also transmission electron microscopy in

156   selected areas. No inlcusions were detected in rutile. One run (RT48) was carried out heating the

157   sample to 600 °C, followed by immediate quenching. For this run (heating-quenching experiment,

158   Table 1) with the shortest possible run time with our equipment we give a value of ~25 min run

159   duration.

160   FTIR spectroscopy

161   *Sample preparation.* Slabs were cut parallel to (110) from the centre of the reacted crystal

162   (Fig. 1) and polished with diamond paste (grain size 1 µm) on both sides. They were successively

163   thinned until the peak-shape of the IR spectra indicated no saturation of the signal. The final

164   uniform thickness of the sections was measured with an optical microscope (Table 1). At least 10

165   points around the rims of the thinned rutile slabs were measured and averaged. The statistical error

166   (1 sd) is <6 % and close to the value of the microscope's calibration of 5 % (from 40 values of a

167   standard slab). We assume as a conservative estimate a 10 % blanket error on the average thickness

168   used in the calculations. We also studied a natural rutile from a retrogressed eclogite *in rock matrix,*

169   which was previously analyzed for trace element zoning (Lucassen et al. 2010, 2011). The H_2O

170   content of this large crystal has been measured by FTIR along a profile. It has a prismatic habit (~

171   25 mm length in c direction and 5 mm diameter; Lucassen et al. 2010) and was cut perpendicular to

172   elongation near the center of the crystal. Orientation was controlled on a thin section with a

173   polarizing microscope. A ~1 mm thick section was prepared from the same slab and, after in-situ

174   trace element analysis by LA-ICP-MS (Lucassen et al. 2010), subsequently thinned to a

6

175   freestanding section of 0.4 mm thickness suitable for transmission FTIR. There is no systematic

176   change of H^+ with proximity to the laser spots, the short-time heating by laser ablation does not

177   influence the result.

178   *Data acquisition.* We collected single-crystal IR spectra on the starting material and the

179   reacted crystals using a Bruker ISF 66v or Vertex 80v spectrometer both attached with a Hyperion

180   microscope. The spectrometers were equipped with a Globar light source, a KBr beamsplitter, and a

181   liquid Nitrogen cooled InSb detector. IR spectra were collected in the range of 2500 to 4000 cm^{-1}

182   and averaged over 512 scans to detect the OH stretching vibrations. Polarized spectra were

183   collected with a KRS5-polarizer with the electrical vector of the polarized radiation **E** parallel and

184   perpendicular to the crystallographic *c*-axis. Spectra were acquired with an aperture of 100 x 100

185   µm at a spectral resolution of 2 cm^{-1}. For the natural crystal the procedure was the same except for a

186   smaller aperture of 50 x 50 $µm^2$ that was chosen to approximate the area covered by laser ablation

187   (LA-ICP-MS) for trace element analyses. Hydrogen in the tetragonal rutile structure occupies an

188   interstitial position at the shared edge of the cation octahedron (Swope et al. 1995). This causes the

189   strong polarization of the OH-absorption with ~100 % absorption in FTIR polarized spectra

190   perpendicular to the *c* axis and little or none parallel *c*. Careful orientation of the slabs under the

191   polarizing microscope revealed >> 99 % of the absorption perpendicular *c* and no analyzable peak

192   was found in the orientation parallel *c*. Therefore, for most measurement points only spectra with **E**

193   perpendicular to *c* were acquired. For quantification, the peak-area was integrated over the same

194   part of the spectrum (wavenumbers 3150 to 3400 cm^{-1}) after subtraction of a linear background for

195   all measurements using the peakfit^R software package. To quantify the H^+ content we calculated the

196   total absorbance of the OH bands by summing up the integral absorbance $A_{i, tot} = 2 A_{i \perp c} + A_{i // c}$.

197   Three different calibrations for the absorption coefficient, ε, of rutile exist. The calibration used in

198   this study (ε = 38,000 l mol^{-1} $_{H2O}$ cm^{-2}; Maldener et al. 2001) results in the lowest H_2O equivalent

199   compared with results from other absorption coefficients (ε = 30,200 l mol^{-1} $_{H2O}$ cm^{-2}, Johnson et al.

200   1973; ε = 6540 l mol^{-1} $_{H2O}$ cm^{-2}, Hammer and Beran 1991). We rely on the calibration of Maldener

201   et al. (2001) because they used (1) nuclear reaction analysis for the analyses of absolute H

202   concentration and (2) polarized spectra in their FTIR analyses. In Table 1, we give the weighted

203   average of the individual data points; for the individual data points the error propagation results in a

204   relative error of 17.6 % and includes the error on ε 38,000±4000 l mol^{-1} $_{H2O}$ cm^{-2} (Maldener et al.

205   2001) and blanket errors of 10 % on the thickness and the fitted peak area of the FTIR signal.

206

207   Raman spectroscopy

7

208   Confocal Raman spectroscopy at GFZ was used to estimate H^+ content of crystals, which

209   were not transparent enough for FTIR (Thomas et al., 2008; 2009), because FTIR analyses cannot

210   be performed in this material without substantial thinning of the slabs. We used a Horiba Jobin-

211   Yvon Labram HR 800 UV-VIS spectrometer (gratins 1800 grooves/mm) in backscattering

212   configuration using a CCD detector, an Ar laser and an Olympus optical microscope with a long

213   working distance 100x objective. For sample excitation, we used the 488 nm Ar line and a laser

214   power of 300 mW. The confocal pinhole of 100 μm was used, which corresponds to a spectral

215   resolution of about 1 cm^{-1}. Raman spectra were acquired in three cycles over 1000 s for unreacted

216   rutile with low water content, and 300 s for reacted rutile with high water content. The H^+ content

217   (~3 ppm H_2O equivalent) of the pure rutile was first quantified by FTIR and then the estimation of

218   H^+ content was made by comparison of the OH Raman-peak areas of unreacted doped rutile with

219   the peak areas of unreacted pure rutile, which were identical. Differences of H^+ contents between

220   reacted Nb (low), pure (medium), Cr (high), and V (no H^+) doped rutile measured by FTIR

221   spectroscopy (see 'Results' below) are also seen in the different signal intensities of Raman spectra

222   of the respective samples (example in Fig. 2e). Therefore we consider this method as useful for

223   comparative estimates between rutile of known and unknown H^+ contents even if we cannot correct

224   for absorption of the incoming and outgoing laser light by the colored samples. Thus, water content

225   could be higher in the untreated Cr and Nb than in the pure rutile, but is still low.

226

227   UV-VIS spectroscopy

228   Optical absorption spectra were measured at room temperature in the range 350-2500 nm

229   (ca. 28570-4000 cm^{-1}) with a single-beam microspectrophotometer constructed from a SpectraPro-

230   275 triple grating monochromator, a highly modified polarizing microscope MIN-8 supplemented

231   with Thompson-Glan polarizing prism, and an IBM PC. Two 10× achromats served as objective

232   and condenser. Changeable photoelectric multiplying tubes and cooled PbS-cell were used as

233   photodetectors. A mechanical high-stabilized 300 Hz chopper and lock-in amplifier were applied to

234   improve the signal/noise ratio. The spectra were scanned with steps $\Delta\lambda$ = 1 nm, 2 nm, 5 nm and 10

235   nm in the range 330-450, 450-1000, 1000-1800 and 1800-2500 nm, respectively. The spectral slit

236   width did not exceed 1 nm in the whole range studied. The diameter of the measuring spot was not

237   larger than 100 μm. To evaluate energy, peak intensity and half-widths of the bands, peakfit^R 4.0

238   (Jandel Scientific) software was used to fit the spectra with Gaussian curves after they were

239   converted to linear wave number scale. Band shapes were assumed to be Gaussian. The absorption

240   background was fitted by a combination of Gaussian and Lorenz.

241

8

242   Heating experiment

243   Diffusion of H^+, O and cations can be an important factor, which possibly influences our

244   results. Therefore, we carried out heating experiments. From run RT40, a Nb-doped synthetic rutile

245   was selected for the experiment. The rutile slab with a (110) orientation of the polished surfaces

246   was placed in the sample-cell of a Linkam TS1500 heating stage limited to 1000 °C. The

247   atmosphere in the cell was dry N_2 throughout the experiment. The crystal was heated from room

248   temperature to 200 °C, held for 10 minutes, and subsequently heated in steps of 50 °C (held three

249   minutes each) to measure an IR spectrum. A new background was measured at 200 °C and after

250   each 100 °C increase, because material properties of the assemblage change with *T*. Unpolarized

251   spectra were acquired over 256 scans with an aperture of 200 x 200 μm^2. Acquisition of background

252   or analyses of rutile including movement of the motorized stage and focusing needs four minutes.

253   For each temperature step, four measurements were performed starting in the centre Z, followed by

254   rim R1 perpendicular to the *a* axis with a face (hk0), rim R2 perpendicular to *c* with a face (00l),

255   and back to Z (Z', see Fig. 6a).

256

257   **Results**

258

259   Under the SEM the polished surface of the reacted rutile shows little effect of dissolution, because

260   solubility of rutile in pure water at given *P* and *T* is low (e.g., Ayers and Watson 1993, Antignano

261   and Manning 2008). The FTIR polarized absorption spectra of all reacted samples (except the V-

262   doped sample, which showed no absorption) show a well-defined single main peak (Fig. 2). The

263   calculated wavenumbers represent the centre of the fitted main peak. In the pure, Fe-doped, and Nb-

264   doped rutile crystals they are around 3278 cm^{-1}, in Cr-doped rutile the wavenumbers tend to be

265   slightly higher at 3279 cm^{-1}. The wavenumbers are within the range of values reported in the

266   literature for H^+ incorporation into rutile (e.g. Johnson et al. 1973, Khomenko et al. 1998; Herklotz

267   et al. 2011).

268   *Pure rutile.* Calculated H^+ contents of pure rutile in time series experiments (~25 minutes to

269   14 days) reveal little compositional variation. Systematic core–rim zoning is absent (Fig. 2). The

270   calculated average H_2O equivalent varies between 271 and 360 ppm (Table 1) with an average

271   value of 314±50 ppm for all six runs with pure or nearly pure crystals, equivalent to $8.87 \cdot 10^{19}$ H cm$^-$

272   ^{3} rutile. There is no clear trend in H^+ concentration to lower contents in the shorter experiments,

273   despite the lowest value of ~270 ppm occurs in the 1 h and the heating-quenching (~25 min)

274   experiments. Excluding these two short-time runs yields an average of 333 ppm, equivalent to

275    $9.44 \cdot 10^{19}$ H cm^{-3} rutile (Table 1). Raman spectroscopy shows the same anisotropy (example for run

9

276 RT30a, see Fig. 2e). The signal of the unreacted sample is very weak, but at the same wave number

277 ~3275 cm^{-1} as the large signal from the reacted sample.

278   During the experiments pure rutile changes color from clear or slightly brownish-yellow

279 (Fe-doped) to deep blue. The polarized UV-VIS spectrum of untreated pure rutile consists of a very

280 steep practically isotropic UV absorption edge, which cuts off the UV light with energies higher

281 than ca. 24,300 cm^{-1} (run RT30a; Fig. 3a). The edge considerably differs in shape from UV-VIS-

282 edges in spectra of oxygen-based minerals caused usually by extremely strong UV-centered ligand-

283 metal charge-transfer bands $O^{2-} \rightarrow Me^{n+}$ (mainly $O^{2-} \rightarrow Fe^{3+}$, Fe^{2+}), which, as a rule, are more

284 gently sloping and distinctly pleochroic. These differences may be due to the fact that in the rutile

285 spectrum the edge is caused by the fundamental absorption, i.e. electronic transitions from the

286 valence to the conduction band. The material is perfectly transparent in the forbidden gap, i.e., in

287 the band gap between valence and conduction bands, at least down to 4000 cm^{-1} (Fig. 3a).

288   After reaction with H_2O, an extremely broad and intense band with a broad maximum at

289 around 6400 cm^{-1} appears in the NIR range aside the UV-absorption edge (Fig. 3b). The high-

290 energy tail of the band covers the low-energy part of the visible range causing, together with the

291 edge, intense blue color and distinct dichroism. The latter is due to the polarization property of the

292 band, which is much stronger in $\mathbf{E}\|\mathbf{c}$- than in $\mathbf{E}\perp\mathbf{c}$-polarization. The curve fitting analysis evidences

293 that the band very likely has a complex structure, consisting of at least two components: in $\mathbf{E}\|\mathbf{c}$-

294 polarization aside the main, stronger band at ~6400 cm^{-1} there is also a relatively weak and broad

295 component with a poorly defined maximum somewhere around 11,000 cm^{-1}. In $\mathbf{E}\perp\mathbf{c}$-polarization its

296 appearance is not so obvious, although judging from its broadness (Fig. 3b) one may assume that it

297 may also be a combination of several bands.

298   In the spectrum of the untreated Fe-doped rutile (run RT30b; Fig. 3c) a broad $\mathbf{E}\|\mathbf{c}$-polarized

299 absorption band appears at around 20,850 cm^{-1} with a width, FWHM, of ~5500 cm^{-1} overlapping

300 the low-energy wing of the absorption edge. It causes a light brownish-yellow color and distinct

301 yellow-colorless dichroism of the sample. After reaction the crystal from run RT30b became dark

302 blue. Its absorption spectrum (not shown) is identical to that of nominally pure rutile (see Fig. 3b).

303 The NIR band at ~ 6400 cm^{-1} is so strong that at a thickness of about 60 μm the band at 20,850 cm^{-1}

304 caused by Fe^{2+}/Ti^{4+} IVCT is not seen. Therefore, it is difficult to decide whether it did disappear at

305 thermal treatment or, simply, is not observable being hidden by much stronger absorption caused by

306 Ti^{3+}/Ti^{4+} IVCT transition.

307   *Nb-doped rutile* shows a uniform distribution of H^+ (Fig. 4a). The average calculated value

308 of H_2O equivalent is ~240 ppm (run RT36; Fig. 4a, Table 1) and ~230 ppm (run RT40, that was

309 used in a heating experiment; see below). These values are the lowest in the sample set. The Nb-

310 doped rutile changed its color from light greenish-blue (untreated) to deep blue ($\mathbf{E}\|\mathbf{c} > \mathbf{E}\perp\mathbf{c}$). The

311 UV-VIS-spectrum of the untreated sample (not shown) displays the high-energy absorption edge

312 and a relatively weak Ti^{3+}/Ti^{4+} IVCT band at ~6400 cm^{-1}, similar to that of a reacted pure rutile

313 (Fig. 3b), though of much lower intensity. In the treated sample the intensity of the Ti^{3+}/Ti^{4+} IVCT

314 band significantly increases thus causing the intense blue color (Fig. 4a).

315   *Cr-doped rutile* yielded an average H_2O equivalent of uniformly distributed ~900 ppm,

316 which is the highest in the entire sample set (RT38; Fig. 4b, Table 1). In the untreated sample an

317 intense slightly dichroic absorption edge in the UV-VIS spectrum was shifted significantly to lower

318 energies compared with the pure rutile (Fig. 5a; cf. Fig. 3a), cuts off violet, blue and green light and

319 thus causes the color and a weak dichroism. Overlapping with the edge is a vague broad absorption

320 band or a system of unresolved bands in the range from ca. 14,000 cm^{-1} to 17,000 cm^{-1}. There is

321 obviously no absorption in the NIR range caused by Ti^{3+}/Ti^{4+} IVCT transition. After reaction it

322 almost retains its brownish-orange color ($\mathbf{E}\|\mathbf{c} \geq \mathbf{E}\perp\mathbf{c}$), but the spectrum shows now a prominent

323 Ti^{3+}/Ti^{4+} IVCT band at ~ 6400 cm^{-1} (Fig 5a,b). The high-energy absorption edge becomes stronger

324 that is seen as a shift to lower energies, and in a thin-enough section the sample acquired a bright

325 orange color. The grayish tint in the untreated sample, which is caused by the absorption between

326 14,000 cm^{-1} and 17,000 cm^{-1}, disappeared. The high-energy absorption edge became stronger that is

327 seen as a shift to lower energies. In the NIR-range the Ti^{3+}/Ti^{4+} IVCT band appears (Fig. 5a,b)

328 though it is relatively weak compared to the reacted pure rutile (Fig. 3b).

329   *V-doped rutile* shows no peaks near the 3277 – 3280 cm^{-1} wave numbers in the polarized

330 FTIR spectra (runs RT37 and RT46) and also in the Raman spectrum there is no indication for an

331 OH-related peak.. We conclude that no appreciable amounts of H^+ were incorporated. Untreated V-

332 doped rutile is black, only in extremely thin sections of ~ 5 µm thickness, the crystals become

333 transparent with a very dark-blue color. They remain black after the run. The main part of the thin

334 foil prepared from reacted rutile (RT37) is dark grayish-red whereas the other parts comprise well

335 distinguishable dark-blue areas embedded randomly in the red matrix of the crystal. Unpolarized

336 spectra of the dark-blue areas of the untreated and reacted rutile are similar and only the spectrum

337 of the reacted rutile is shown (Fig. 5c). It comprises a high-energy edge and the wing of a strong

338 absorption in the low-energy part of the spectra. This forms a deep narrow window of transmittance

339 in the range 25,000 – 20,000 cm^{-1}, which causes the dark-blue color. The rutile contains high

340 concentration of Ti^{3+}, because the strong absorption, making the foil totally opaque at energies

341 lower than ca. 15,000 cm^{-1}, is very likely caused by Ti^{3+}/Ti^{4+} IVCT around 6400 cm^{-1} (see above).

342 The spectrum of the grayish-red material consists of a strong high-energy absorption edge

11

343   overlapping two broad bands with maximum at around 18,000 cm^{-1} and 8000 cm^{-1}, the former one

344   is likely a superposition of at least two components (Fig. 5c).

345   *Heating experiment.* For this experiment we used the Nb-doped crystal from run RT40,

346   which has an average H_2O equivalent at ambient *T* after reaction of 229 ppm ±19 (1s, n = 18),

347   uniformly distributed in the crystal. At the three measuring sites it has in the centre 210 ppm, at the

348   rim towards the a-axis (hk0) 235 ppm and at the rim towards the c axis (00l) 250 ppm. Results of

349   the experiment are given in Figure 6. The H_2O contents vary within and between the measurement

350   sites; a slight but unsystematic decrease is observed before reaching 350 °C (Fig. 6). The average of

351   the four measurements is near 180 ppm. Significant deprotonation starts between 350 and 400 °C

352   and is finished between 550 and 600 °C. No signal from OH can be discerned at 600 and 650 °C.

353   Color change occurs concurrently from deep blue to greenish blue of H^+-free Nb-doped rutile. From

354   22 °C to 450 °C, the transmission signal of IR light (amplitude) is variable but low with most values

355   between ~130 and ~200. It shows a sharp increase at and above 450 °C, when H^+ leaves the rutile.

356

357   **Discussion**

358

359   <u>Pure rutile</u>

360   Titanium in stoichiometric TiO_2 is Ti^{4+}. The pure rutile and the crystals with traces of Fe represents

361   such stoichiometric TiO_2, because the starting material was treated in O_2 atmosphere at high T and

362   is fully oxidized. Non-stoichiometric rutile compositions (e.g. Liborio and Harrison 2008) can't be

363   ruled out completely, but are likely of minor importance.

364   The likely mechanism of H^+ incorporation is a charge transfer reaction including the

365   reduction of Ti and charge balance by incorporation of H^+, which is proved by the presence of a

366   strongly polarized OH band. Because the sample contains no other transition metal ions but Ti, the

367   band is most probably caused by electronic $Ti^{3+} + Ti^{4+} \rightarrow Ti^{4+} + Ti^{3+}$ intervalence charge-transfer

368   transition (Ti^{3+}/Ti^{4+} IVCT) between the ions in edge-shared octahedral sites of the structure (cf.

369   Khomenko et al. 1998). The charge misbalance caused by partial reduction $Ti^{4+} \rightarrow Ti^{3+}$ is

370   compensated by H^+, which enter the structure during reaction with H_2O and form (OH) with the

371   neighboring oxygens.

372   In crystals with the probable presence of a certain content of Fe, the band is likely caused by

373   electronic IVCT transition between Fe^{2+} (which substitutes Ti^{4+} in octahedral positions) and Ti^{4+} in

374   neighboring sites (cf. e.g. Burns 1993). The charge misbalance caused by $Ti^{4+} \rightarrow Fe^{2+}$ substitution

375   is most likely compensated by H^+ (~3 ppm H_2O) bonded to oxygen to form hydroxyl ions. The

376   strict **E**||c-polarization of the band causes a distinct yellow-colorless dichroism of the sample and

12

377   indicates Fe^{2+}/Ti^{4+} IVCT between the ions occupying adjacent edge-sharing sites within octahedral

378   chains elongated along the **c**-axis. To our knowledge there is only one publication where a Fe^{2+}/Ti^{4+}

379   IVCT band was observed on synthetic material: Khomenko et al. (1994) interpreted a broad

380   absorption band at 23,000 cm^{-1} in spectra of synthetic Fe-Ti-bearing garnet as electronic Fe^{2+}/Ti^{4+}

381   charge-transfer transition between the ions in adjacent dodecahedral and octahedral sites. Rutile

382   from run RT30b is, very likely, the second example. As a weak admixture of Fe is likely present,

383   there is no doubt that the broad band at 20,850 cm^{-1} is related to the Fe-content. Together with high

384   Ti^{4+}-concentration in the sample this is strong evidence for attribution of such bands in optical

385   absorption spectra of natural Fe-Ti-bearing minerals to electronic Fe^{2+}/Ti^{4+} IVCT transitions.

386   At 600 °C diffusion of H^+ in rutile (Johnson et al. 1975) is reasonably fast to facilitate an

387   IVCT reaction. In contrast, diffusion coefficients for cations (Van Orman and Crispin 2010) and

388   oxygen (Dennis and Freer 1993) in rutile indicate that at 600 °C and duration of the experiments

389   they do not move significantly in relation to the volume of the crystals. The reduction of Ti^{4+} to Ti^{3+}

390   in dependence on f_{O2} is well known from the phase relations in the H_2O-free system Ti–O

391   (Wahlbeck and Gill 1966) and described as Ti_nO_{2n-1} compounds (Magnéli phases; e.g., Andersen et

392   al. 1957) under O-deficient conditions, e.g., in synthetic rutile crystals grown from a melt. For

393   hydrothermal conditions the dependence of reduction of Ti in pure rutile on f_{O2} has been

394   experimentally investigated (Colasanti et al. 2011). Reduction of Ti^{4+} to Ti^{3+} causes the blue color

395   (e.g., Khomenko et al. 1998) and hence a characteristic absorption band in the UV-VIS spectra (Fig.

396   3). Furthermore, Khomenko et al. (1998) showed in a heating experiment that the UV-VIS

397   absorption band (Ti^{4+}-Ti^{3+}) and the FTIR absorption band (interstitial H^+) vanish concomitantly

398   during heating. The saturation level for H^+ therefore also refers to the saturation level for Ti^{3+} in the

399   pure rutile, equivalent to $8.87 \cdot 10^{19}$ Ti cm^{-3} rutile, or $9.44 \cdot 10^{19}$ Ti cm^{-3} rutile excluding the short-time

400   runs (average value, individual values see Table 1).

401   The uniform distribution of H^+ in the crystals indicate that diffusion of H^+ in rutile is not a

402   limiting factor of H^+ incorporation or loss in rutile at the given temperature, H_2O-pressure, time,

403   size and shape of the specimens. This is supported by the results of the heating experiment at

404   atmospheric pressure, which showed no substantial loss of H^+ in the centre of the crystal up to

405   450°C (Fig. 6). Although under ambient pressure the diffusion of H^+ in rutile is fast parallel to the

406   crystallographic *c* direction and slow perpendicular to *c* (Johnson et al. 1975), the 60 μm x 1800 μm

407   large crystal plate likely deprotonates during the heating experiment along the slow diffusion path ⊥

408   *c*. For a measurement-cycle duration of 13 minutes the calculated out-diffusion length ⊥ *c* is 11 μm,

409   19 μm, and 32 μm at 500, 550 and 600°C respectively, compared to the half thickness ⊥ *c* of 30 μm

410   (diffusion coefficients from Johnson et al. 1975). The diffusion length ‖ *c* is ~210 μm at 600 °C,

13

411 which is small in comparison with the half length of 900 µm extension of the crystal ||c. Although at

412 600 °C only a very short time is required to reach the H-saturation level for the high-pressure

413 experiments, the rapid quenching to a temperature below 450 °C within ~1 min ensures that the H^+

414 content is preserved. At 600 °C the out-diffusion length of H^+ would be ~65 µm ||c and ~10 µm $\perp c$.

415 This is very small compared to the 1000 x 2000 µm large crystals. In the absence of a systematic

416 compositional zoning we assume saturation of the H^+ contents in the rutile crystals. For pure rutile,

417 the best value for the saturation at 600°C and 400 MPa P_{H2O} is accepted as 314 ± 50 ppm; the

418 averages of individual runs range from 270 to 370 ppm (Table 1). This rather uniform H^+

419 concentration from all experiments is a direct measure for the amount of Ti^{3+} and indicates well-

420 reproducible run conditions. The relatively large difference in the ionic radii of Ti^{3+} (0.67 Å) and

421 Ti^{4+} (0.605 Å) limits the incorporation of H^+.

422   Experiments by Colasanti et al. (2011) result in lower H_2O than observed in ours. At 1 GPa,

423 600 °C, and f_{O2} controlled by NNO they determined values near or below 160 ppm and calculated

424 <200 ppm from thermodynamic data. At 600°C the major differences between the two data sets are

425 the longer run times, lower pressure, and buffering of f_{O2} in our experiments by the autoclave

426 material. The longer run times have no influence, because H^+ diffusion is fast; volume and

427 dimensions of rutile are similar in both sets of experiments. The H^+ incorporation is moderately

428 pressure dependent (Colasanti et al. 2011) and using their data the calculated H_2O at 400 MPa,

429 600°C, at NNO-buffering is ~ 160 ppm, i.e. the half of our average measured value. According to

430 the calibration of Colasanti et al. (2011) the f_{O2} conditions in our experiments were more reducing

431 than conditions provided by the autoclave material and near to the Co-CoO buffer.

432

433 <u>Trace element doped rutile</u>.

434 The following discussion relies on the analyzed concentrations of dopants and H^+ (Table 1) and the

435 results from UV-VIS spectroscopy. We assume charge balance in both the initial and reacted rutile

436 and substitution of Ti^{4+} at the octahedral site. Differences of ionic radii between dopants and Ti^{4+}

437 should be small to avoid stress due to lattice mismatch; however, ionic radii vary with oxidation

438 state (Shannon 1976; see Table 1) and the oxidation states at common geological conditions of the

439 dopants Nb^{5+}, Cr^{3+} and V^{5+} can possibly also change during the hydration experiment.

440   *Nb-doped rutile* (500 ppm, equivalent to $1.4 \cdot 10^{19}$ Nb cm^{-3} rutile; Table 1) in the untreated

441 state shows the Ti^{3+}/Ti^{4+} IVCT band, indicating the presence of Ti^{3+} and an oxidation state of Nb^{5+}

442 with an ionic radius of 0.64 Å in octahedral coordination, which fits quite well to the ionic radius of

443 0.605 Å for Ti^{4+}. Charge balance for Nb^{5+} is achieved by reduction of an equivalent of Ti^{4+} to Ti^{3+}

444 (0.67 Å). At low doping levels ($\sim Ti_{0.99}Nb_{0.01}O_2$) all Nb has been demonstrated to be Nb^{5+} charge

445 balanced by Ti^{3+} whereas at high concentrations isovalent Nb^{4+} substitutes for Ti^{4+} (e.g. Morris et

446 al. 2000; Di Valentin et al. 2009). After reaction with H_2O the Ti^{3+}/Ti^{4+} IVCT band grew

447 significantly and the very intense dark-blue color is accompanied by H^+ incorporation. There is no

448 spectroscopic proof that Nb^{5+} was reduced to Nb^{4+} during this reaction, as the intensity of a possible

449 absorption band of electronic spin-allowed *dd*-transition of Nb^{4+} ($4d^1$-configuration) may be too low

450 to be distinguished from the strong absorption caused by the Ti^{3+}/Ti^{4+} IVCT process. The

451 persistence of Nb^{5+} after reaction could explain the low H_2O content of 240 ppm in the Nb-doped

452 rutile. 500 ppm Nb are equivalent to $1.4 \cdot 10^{19}$ atoms cm^{-3}, or $6.88 \cdot 10^{19}$ H^+ cm^{-3} rutile (Tab. 1) and

453 require reduction of the same amount of Ti^{4+} to Ti^{3+}. Considering the saturation level of Ti^{3+}

454 formation (the H_2O equivalent of ~314 ppm, or the average value of $8.87 \cdot 10^{19}$ atoms Ti resp. H cm^{-3}

455), 240 ppm of H_2O equivalent account for the reduction of Ti^{4+} to Ti^{3+}.

456   *Cr doped* rutile (2000 ppm equivalent to $9.8 \cdot 10^{19}$ H cm^{-3} rutile; Table 1) shows a large

457 excess of H_2O (~900 ppm, equivalent to $2.57 \cdot 10^{20}$ Cr cm^{-3}) compared to the saturation level for Ti^{3+}

458 (Fig. 4b). It is surprising that relatively weak changes in optical absorption spectra are accompanied

459 by the highest H^+ incorporation. Therefore the high content of OH in the reacted sample is probably

460 connected with a valence change of Cr rather than with that of Ti. At common geological

461 conditions, Cr has two preferred oxidation levels 6^+ and 3^+, but can also occur as Cr^{4+} and Cr^{2+}.

462   A possible explanation for the high H_2O incorporation in the Cr-doped rutile is isovalent

463 replacement of Ti^{4+} by Cr^{4+} in the starting material. Koopayeh et al. (2010) also argued that in

464 synthetic single crystal rutile, Cr is incorporated at low doping levels of ~2 at% as Cr^{4+} instead of

465 Cr^{3+} at higher contents. On the other hand, this contradicts the results derived by other investigators

466 who believe that Cr^{3+} does contribute to yellow coloration of Cr-bearing TiO_2-pigments. For

467 example, Ishida et al. (1990) studied powdered Cr-doped rutile by electron spin resonance and

468 diffuse reflectance spectroscopy and arrived at the conclusion that Cr^{3+} and Cr^{4+} form solid

469 solutions with TiO_2 and, depending on Cr content, cause yellow and orange colors of the pigments,

470 respectively. As no spectroscopic evidence of Cr^{3+} was observed in the untreated and reacted

471 sample, we speculate that most Cr^{4+} is reduced to Cr^{2+} that is charge balanced by H^+. Reduction

472 from Cr^{4+} to Cr^{2+} would account for ~700 ppm H_2O equivalent leaving the remaining 200 ppm to

473 Ti^{3+}/Ti^{4+} IVCT. Absorption spectra of Cr^{3+} (electronic configuration $3d^3$) are very well studied in

474 many oxygen-based minerals and compounds (e.g., Burns 1993): in the visible range Cr^{3+} always

475 causes two broad intense spin-allowed dd-bands $^4A_{2g} \rightarrow {}^4T_{2g}$ and $^4A_{2g} \rightarrow {}^4T_{2g}$, frequently

476 complicated by superimposing weaker and sharper absorption lines, caused by electronic spin-

477 forbidden dd-transitions of Cr^{3+}, and, depending on mean Cr–O distance and thus on crystal field

478 strength of Cr^{3+} in CrO_6-octahedra, induces an intense green to red color. But, as emphasized above,

479   no but absorption features, which can be assigned to the *dd*-transitions of Cr^{3+}, are seen in the

480   spectra of both initial and treated Cr-doped rutile (Fig. 5). On this account we are forced to adopt a

481   disputable interpretation that in Cr-doped rutile Cr^{4+} reduces immediately to Cr^{2+} without passing

482   through its trivalent state. The existence of Cr^{2+} in geological material has been debated in lunar

483   rocks, i.e. at extremely reducing conditions (e.g., Mao and Bell 1975) and is known in melts as

484   unstable under ambient conditions (e.g., Berry et al., 2006). It is also known from high-pressure

485   synthetic minerals (Furche and Langer, 1998).

486   Spectroscopic evidence for the presence of Cr^{4+} and Cr^{2+} in the reacted Cr-doped rutile is

487   difficult because Cr^{4+} is very rare in minerals and compounds, so that its absorption spectra are

488   almost unknown. By analogy with V^{3+} (electronic configuration d^2) one may assume that the weak

489   and broad absorption envelope between 14,000 cm^{-1} and 17,000 cm^{-1} is a combination of two or

490   three spin-allowed bands, caused by spin-allowed electronic transitions $^3T_{1g}$ $(^3F) \rightarrow {}^3T_{2g}$ $(^3F), \rightarrow$

491    $^3T_{1g}$ (^3P) and $\rightarrow {}^3T_{1g}$ (^3F). We assume that the lower-energy shift of the absorption edge may be

492   due to UV-absorption caused by electronic ligand-metal charge-transfer transition $O^{2-} \rightarrow Cr^{4+}$.

493   Probably, it occurs at lower energies than the edge of fundamental absorption caused by electronic

494   transitions between the valence band (mostly composed by electronic levels of O^{2-}) to the transition

495   band (mostly of Ti^{4+}) and thus extends to the visible range in spite of the low Cr content. The

496   absorption envelope at 14,000 cm^{-1} to 17,000 cm^{-1}, which covers a significant part of the visible

497   range and causes greyish tints in the crystal color, may be attributed to electronic *dd*-transitions of

498   Cr^{4+} in octahedral coordination.

499   The reaction with H_2O affected the valence of both Ti and Cr. The absorption edge in the

500   reacted sample caused by ligand-metal charge-transfer transition $O^{2-} \rightarrow Cr^{4+}$, shifts noticeably to

501   lower energies, whilst the band(s) at around 16,000 cm^{-1} to 17,000 cm^{-1} that are assigned to Cr^{4+},

502   disappear (Fig. 5b). Instead, there again appears a relatively weak and broad NIR band of Ti^{3+}/Ti^{4+}

503   IVCT with a maximum around 6500 cm^{-1}. The weak unpolarized band with a maximum at ~13,500

504   cm^{-1} on its low-energy wing can be attributed to the *dd*-transition of Cr^{2+} in octahedral coordination.

505   The spectra of Cr^{2+} (d^4) are also rather poorly studied to be sure that the band is really caused by a

506   spin-allowed transition of Cr^{2+}. In the spectrum of Cr_2SiO_4, studied by Furche and Langer (1998),

507   the most intense bands appear at 15,700 cm^{-1} and 18,700 cm^{-1}, i.e., at much higher energies than in

508   our case.

509   *V-doped* rutile (2000 ppm, equivalent to $1.0\cdot10^{20}$ V cm^{-3}) has no H^+ incorporated according

510   to FTIR spectra. Charge balance of $2Ti^{4+} = V^{5+} + Ti^{3+}$ for 2000 ppm V^{5+} would be equivalent to

511   ~350 ppm H_2O, which is already the saturation level of Ti^{3+}. Consequently, no H^+ can be

512   incorporated into rutile. As there is no evidence of H-content in both, initial and reacted V-doped

16

513   rutile, it is difficult to decide what mechanism maintains the relatively high concentration of Ti^{3+}.

514   One may assume that during the reaction V^{5+} is reduced to V^{4+}, whilst Ti^{3+} oxidizes back to Ti^{4+},

515   seen as the partly transformation of blue rutile into the red material. Such model is consistent with a

516   lack of Ti^{3+}/Ti^{4+} IVCT band in the NIR of the red parts of the reacted rutile. The two broad bands at

517   approximately 7500 cm^{-1} and 18,500 cm^{-1} may be caused by spin-allowed transitions in V^{4+}. In

518   crystal compounds V^{4+} is commonly present as vanadyl $[VO]^{2+}$ cation. It is one of the most stable

519   diatomic ions known, which forms a wide range of complexes. However, vanadyl-bearing minerals

520   are rather rare. Usually they are colored in various hues of blue and green, and their electronic

521   spectra rather differ from what we observe in the V-bearing red rutile (cf. e.g. Platonov 1976).

522   Nevertheless, in case of the red rutile we can hardly imagine another explanation of the spectrum

523   than V^{4+} in octahedral sites though more detailed assignment of the absorption bands is hardly

524   possible. Also, it is difficult to explain why a perfectly homogeneous blue V^{5+}-bearing rutile

525   transformed only in part into red V^{4+}-bearing rutile whilst some parts of the crystal maintained the

526   initial dark-blue color and strong Ti^{3+}/Ti^{4+} IVCT band. In any case, neither the red nor the blue

527   parts contain H^+. Note that in natural V-bearing rutile annealing in argon at 973 K and 1173 K

528   induces an increased absorption in the visible range (Luo et al. 2012) that is seen in diffuse

529   reflectance spectra as a growing broad shoulder band from 400 to 600 nm (25,000 to 16,700 cm^{-1})

530   similar to that observed in the absorption spectrum of the red material in the treated sample (Fig.

531   5c). Luo et al. (2012) also explain this by the increased content of V^{4+}, which is believed appearing

532   due to reduction of V^{5+} to V^{4+} during the thermal treatment.

533

534   **Observations on natural rutile - geological implications**

535   To explore the possible use of H-in-rutile as a geohygrometer (Vlassopoulos et al. 1993),

536   geothermobarometer and oxybarometer (Colasanti et al. 2011), we measured the H^+ content in a

537   natural rutile. Molecular H_2O was not detected in the IR spectra and all H^+ is bound to oxygen of

538   the TiO_2 lattice in line with the observations by Swope et al. (2005). The calculated wavenumbers

539   that represent the centre of the fitted peak, are near 3280 cm^{-1} and similar to those of our synthetic

540   rutile and values reported in the literature (e.g. Johnson et al. 1973, Khomenko et al. 1998; Herklotz

541   et al. 2011). Most H_2O-contents (Fig. 7; Table 2) vary between 400 and 800 ppm with a few higher

542   (up to ~900 ppm) and lower values (down to ~200 ppm). Iron, Nb and Zr contents were analyzed

543   previously along a nearby profile by LA-ICP-MS, with the most abundant trace element being Fe,

544   followed by an order of magnitude less abundant Nb and Zr (Fig. 7; Lucassen et al. 2010). The Nb-

545   and Zr-profiles show a very homogeneous distribution with strongly increasing contents in the outer

546   rims toward a reaction rim of titanite (Fig. 7b). The increasing contents were caused by

547   consumption of rutile by titanite and in-diffusion of Nb and Zr (Lucassen et al., 2010, 2011). In

548   contrast, Fe contents are variable between 2500 and 5000 ppm and Fe is in fact a minor element

549   rather than a trace element (Fig. 7b).

550   We assume the same relation between H_2O and trace element contents as in the synthetic

551   crystals. The dominant replacement in the natural rutile is Ti^{4+} by Fe^{3+} in octahedral coordination

552   plus local charge balance by introducing H^+ at oxygen interstitials (e.g., Vlassopoulos et al. 1991;

553   Bromiley et al. 2005). Isovalent substitution $Zr^{4+} = Ti^{4+}$ has no influence on the H^+ and/or Fe

554   content. If Nb is incorporated as Nb^{5+} and charge balanced by Fe^{3+}, ~420 ppm Fe^{3+} are required to

555   charge balance the maximum amount of Nb^{5+} of 700 ppm, i.e. the possible influence of Nb on

556   available (not charge balanced) Fe^{3+} is moderate considering the high Fe contents. Thus, the

557   measured H_2O contents towards and at the rims grossly follow the Fe contents (Fig. 7b). The

558   calculated $H_2O_{(Fe)}$ equivalent that is hypothetically required for charge balance of Fe^{3+} (corrected

559   for Nb^{5+}) and $H_2O_{(IR)}$ contents measured by FTIR spectroscopy from nearby spots are in fairly good

560   agreement (Fig. 7c,d; Table 2). In 24 of 34 $H_2O_{(IR)}$ - $H_2O_{(Fe)}$ pairs the $H_2O_{(Fe)}$ is higher than $H_2O_{(IR)}$

561   by up to +95% with an average deviation of +31% from $H_2O_{(IR)}$. Ten $H_2O_{(Fe)}$ values are lower than

562   nearby $H_2O_{(IR)}$ with an average deviation from $H_2O_{(IR)}$ –16%. The assignment of an uncertainty to

563   the independent estimates of $H_2O_{(IR)}$ and $H_2O_{(Fe)}$ remains tentative, because e.g. Fe contents are

564   irregularly distributed in the sample and the FTIR spots are only nearby and not identical with the

565   LA-ICP-MS spots. Within an arbitrarily assigned error of 15%, most $H_2O_{(IR)}$ - $H_2O_{(Fe)}$ pairs overlap

566   (Fig. 7c). The data indicate that large amounts of Fe^{3+} are incorporated by the substitution $Ti^{4+}O_2$ +

567   e^- + H^+ = $Fe^{3+}OOH$. However, we cannot account for possible O vacancies. The same observation

568   was made by Bromiley et al. (2004), who argued that Fe incorporation could be charge-balanced by

569   oxygen vacancies, similar to the incorporation mechanism proposed for Al in Al-doped rutile

570   (Gesenhues and Rentschler 1999).

571   On a geological time scale of several million years from eclogite- to amphibolite facies

572   conditions and final uplift (e.g., Krogh Ravna and Roux, 2006) the natural rutile preserved a

573   correlated zoning of Fe and H_2O, i.e. of a large cation with slow diffusion (approximately 4 orders

574   of magnitude slower than H^+; Sasaki et al. 1985) and the small H^+. Our experiments show that at

575   600 °C (common temperatures in the deeper crust), the observed H^+ incorporation into rutile by a

576   charge transfer reaction occurs within hours; the annealing experiments at atmospheric oxygen

577   pressure of Khomenko et al. (1998) indicate that the reversal of the reaction occurs at temperatures

578   as low as 200°C also within a few hours. Our heating experiment with Nb-doped rutile in N_2

579   atmosphere also shows a rapid release of H^+ between 450 to 550 °C. The H^+ content in minerals

580   with a reaction history on the geological time scale is unlikely to represent the preserved amount of

581   H^+ at high-grade metamorphic conditions due to coupled reduction-oxidation and hydration-

582   dehydration (IVCT plus H^+ diffusion). Oxygen fugacity and H^+ activity are *P-T*-dependent and they

583   will likely start to re-equilibrate, because the reactions are very fast. However, the trace element

584   zoning of the natural rutile was generated during the amphibolite facies retrogression and the in-

585   diffusion of Nb and Zr is closely linked to the growth of titanite at expense of the rutile (Lucassen et

586   al. 2010, 2011). We observe that the $Fe^{3+}OOH$ configuration in the lattice is apparently stable and

587   allows for adjustment to lower H_2O concentrations at the rutile's left rim by the diffusion of Fe^{3+},

588   whereas in the core of the crystals the contents of H_2O are still higher (Fig. 7b). This means that the

589   oxidation state of Fe did not change during the reaction history. The pronounced increase of Nb at

590   this rim of the rutile where Fe decreases may indicate counterdiffusion of the two elements.

591   However, diffusion coefficients of Fe (Sasaki et al. 1985) are about 6 orders of magnitude faster

592   than those of Nb (Sheppard et al. 2007), Zr (Cherniak et al. 2007), and oxygen (Dennis and Freer,

593   1993). The observations indicate that the preservation of H^+ contents in this natural rutile is a

594   complicated interplay of diffusive reequilibration of fast H^+, slower Fe and very slow other trace

595   elements.

596   We conclude (1) that substituting elements in rutile strongly influence the amount of H^+,

597   which can be incorporated into rutile. We also conclude (2) that charge transfer reactions like the

598   observed $Ti^{4+}O_2 + e^- + H^+ = Ti^{3+}OOH$ in the experiments are very fast in pure rutile, and (3) likely

599   transitional in natural rutile with a complex spectrum of minor (Fe) and trace elements such as Nb,

600   V, Cr. The amount of H^+ does not survive geological time scales or at least record a late stage of the

601   thermal and fO_2 evolution. The experiments illustrate the interaction of variably charged cations,

602   e.g., Nb^{5+} and V^{5+} occupy possible Ti^{3+} sites for charge balance that are not available for the above

603   reaction, whereas Cr is obviously reduced similarly as Ti and allows the incorporation of additional

604   H^+. (4) If the oxidation states of trace elements in the rutile are stable, H^+ content relates to charge

605   balance and depends only on the trace element contents. Interpretation in terms of changing fO_2 or

606   H_2O activity is impossible.

607

608

609

610   **Acknowledgements**

611

618
619   **References**
620

621   Andersson, S., Kollen, B., Kuylenstierna, U., and Magnéli, A. (1957) Phase analysis studies on the
622   titanium-oxygen system. Acta Chemica Scandinavica, 11, 1641-1652.

623
624   Antignano, A. and Manning, C.E. (2008) Rutile solubility in H_2O, H_2O-SiO_2 and H_2O-$NaAlSi_3O_8$ at
625   0.7–2.0 GPa and 700–1000 °C: Implications for mobility of nominally insoluble elements in
626   geologic fluids. Chemical Geology, 255, 283-293.

627
628   Ayers, J.C. and Watson, E.B. (1993) Rutile solubility and mobility in supercritical aqueous fluids.
629   Contributions to Mineralogy and Petrology, 114, 321-330.

630
631   Bell, D.R., and Rossman, G.R. (1992) Water in the earth's mantle: The role of nominally anhydrous
632   minerals. Science, 255, 139l-1397.

633
634   Berry, A.J., O'Neill, H.St.O., Scott, D.R., Foran, G.J., and Shelly, J.M.G. (2006) The effect of
635   composition on Cr^{2+}/Cr^{3+} in silicate melts. American Mineralogist, 91, 1901-1908.

636
637   Bromiley, G.D. and Hilaret, N. (2005) An investigation of hydrogen and minor element
638   incorporation in synthetic rutile. Mineralogical Magazine, 69, 345-358.

639
640   Bromiley, G.D., Hilaret, N., and McCammon, C. (2004) Solubility of hydrogen and ferric iron in
641   rutile and TiO_2 (II): Implications for phase assemblages during ultrahigh-pressure metamorphism
642   and for the stability of silica polymorphs in the lower mantle. Geophysical Research Letter, 31,
643   doi:10.1029/2004GL019430.

644
645   Burns, R.G. (1993) Mineralogical Applications of Crystal Field Theory, 2nd edition,
646   551 p. Cambridge University Press, U.K

647
648   Chen, X. and Mao, S. (2007) Titanium dioxide nanomaterials: synthesis, properties, modifications,
649   and applications. Chemical Review 107, 2891−2959.

650
651   Cherniak, D.J., Manchester, J., and Watson, E.B. (2007) Zr and Hf diffusion in rutile. Earth and
652   Planetary Science Letters, 261, 267-279.

653
654   Colasanti, C.V., Johnson, E.A., and Manning, C.E. (2011) An experimental study of OH solubility
655   in rutile at 500–900 °C, 0.5–2 GPa, and a range of oxygen fugacities. American Mineralogist, 96,
656   1291-1299.

657
658   Dennis, P.F. and Freer, R. (1993) Oxygen self-diffusion in rutile under hydrothermal conditions.
659   Journal of Materials Science, 284, 804-4810.

660
661   Di Valentin, C., Pacchioni, G., and Selloni, A. (2009) Reduced and n-type doped TiO_2: Nature of
662   Ti^{3+} species. Journal of Physical Chemistry C 113, 20543–20552.

663
664   Fujishima, A. and Honda, K. (1972) Electrochemical photolysis of water at a semiconductor
665   electrode. Nature, 238, 37–38.

666

667 Furche, A. and Langer, K. (1998) Polarized electronic absorption spectra of Cr_2SiO_4 single crystals.
668 Physics and Chemistry of Minerals, 25, 393-400.

669

670 Gesenhues, U. and T. Rentschler (1999), Crystal growth and defect structure of Al^{3+}-doped rutile,
671 Journal Solid State Chemistry, 143, 210– 218.

672

673 Hammer, V. and Beran, A. (1991) Variations in the OH concentrations of rutile from different
674 geological environments. Mineralogy and Petrology, 45, 1-9.

675

676 Herklotz, F., Lavrov, E.V., and Weber, J. (2011) Infrared absorption of the hydrogen donor in
677 rutile TiO_2. Physical Review, B 83, 235202.

678

679 Johnson, O.W., DeFord, J., and Shaner, J.W. (1973) Experimental technique for the precise
680 determination of H and D concentration in rutile (TiO_2). Journal of Applied Physics, 44, 3008-3012.

681

682 Johnson, O.W., Paek, S.H., and DeFord, J.W. (1975) Diffusion of H and D in TiO_2: Suppression of
683 internal fields by isotope exchange. Journal of Applied Physics, 46, 1026-1033.

684

685 Katayma I., Nakashima, S., and Yurimoto, H. (2006) Water content in natural eclogite and
686 implication for water transport in the deep mantle. Lithos, 86, 245-259.

687

688 Khomenko, V., Langer, K., Rager, H., and Fett, A. (1998) Electronic absorption by Ti^{3+} ions and
689 electronic delocalization in synthetic blue rutile. Physics and Chemistry of Minerals, 25, 338–346.

690

691 Khomenko, V. M., Langer, K., Andrut, M., Koch-Müller, M. and Vishnevsky A. A. (1994) Single
692 crystal absorption spectra of synthetic Ti, Fe-substituted pyropes. Physics and Chemistry of
693 Minerals, 21, 434-440.

694

695 Koohpayeh, S.M., Williams, A.J., Abell, J.S., Lim, J. and Blackburn, E. (2010) Cr-doped TiO_2
696 (rutile): Ferromagnetism in bulk form? Journal of Applied Physics, 108, doi: 10.1063/1.3490997

697

698 Krogh Ravna, E.J.K. and Roux, M.R.M. (2006) Metamorphic evolution of the Tønsvika eclogite,
699 Tromsø Nappe — evidence for a new UHPM province in the Scandinavian Caledonides.
700 International Geology Review, 48, 861-881.

701

702 Ishida, S., Hayashi, M., and Fujimura, Y. (1990) Spectroscopic study of the chemical state and

703 coloration of chromium in rutile. Journal of the American Ceramic Society, 73, 3351-55.

704

705 Liborio, L., and Harrison, N. (2008) Thermodynamics of oxygen defective Magnéli phases in rutile:
706 A first-principles study. Physical Review B77, DOI: 10.1103/PhysRevB.77.104104

707

708 Lucassen, F., Dulski, P., Abart, R., Franz, G., Rhede, D., and Romer, R.L. (2010) Redistribution of
709 HFSE elements during rutile replacement by titanite. Contributions Mineralogy and Petrology, 160,
710 279-295.

711

712 Lucassen, F., Franz, G., Dulski, P., Romer, R.L., and Rhede, D. (2011) Element and Sr isotope
713 signatures of titanite as indicator of variable fluid composition in hydrated eclogite. Lithos, 121, 12-
714 24.

715

21

716 Luo, Z., Lu, A., Li, Y., Zhuang, W., Wu, J., Qin, S., and Wang, C. (2012) Enhanced visible-light
717 response of natural V-bearing rutile by annealing under argon. European Journal of Mineralogy, 24,
718 551–557.
719
720 Maldener, J., Rauch, F., Gavranic, M., and Beran, A. (2001) OH absorption coefficients of rutile
721 and cassiterite deduced from nuclear reaction analysis and FTIR spectroscopy. Mineralogy and
722 Petrology, 71, 21-29.
723
724 Mao, H.K. and Bell, P.M. (1975) Crystal-field effects in spinel: oxidation states of iron and
725 chromium. Geochimica et Cosmochimia Acta, 39, 865-874.
726
727 Morris, D., Dou, Y., Rebane, J., Mitchell, C.E.J., Egdell, R.G., Law, D.S.L., Vittadini, A. and
728 Casarin, M. (2000) Photoemission and STM study of the electronic structure of Nb-doped TiO_2.
729 Physical Review B, 61,13445-13457
730
731 Platonov, A.N. (1976) Nature of color of minerals. Kiev, Naukova Dumka.
732
733 Pouchou, J.L. and Pichoir, F. (1984) Un nouveau modèle de calcul pour la microanalyse
734 quantitative par spectrométrie de rayons X. La Recherche Aérospatiale, 3, 167-192.
735
736 Sasaki, J., Peterson, N.L., and Hoshino, K. (1985) Tracer impurity diffusion in single-crystal rutile
737 (TiO_{2-x}). Journal of Physics and Chemistry of Solids, 46, 1267-1283.
738
739 Schmidt, A., Weyer, S., John, T., and Brey, G.P. (2009) HFSE systematics of rutile-bearing
740 eclogites: New insights into subduction zone processes and implications for the earth's HFSE
741 budget. Geochimica et Cosmochimica Acta, 73, 455-468.
742
743 Shannon R. D. (1976) Revised effective ionic radii in oxides and fluorides. Acta Crystallographica
744 A32, 751-757.
745
746 Sheppard, L.R., Atanacio, A.J., Bak, T., Nowotny, J., and Prince, K.E. (2007) Bulk Diffusion of
747 Niobium in Single-Crystal Titanium Dioxide. The Journal of Physical Chemistry B, 111, 8126-
748 8130.
749
750 Soffer, B.H. (1961) Studies of the Optical and Infrared Absorption Spectra of Rutile Single
751 Crystals. The Journal of Chemical Physics, 35, 940-945.
752
753 Swope, R., Smyth, J., and Larson, A. (1995) H in rutile compounds: I. Single-crystal neutron and
754 X-ray diffraction study of H in rutile. American Mineralogist, 80, 448-453.
755
756 Thomas, S.-M., Thomas, R., Davidson, P., Reichart, P., Koch-Müller, M., and Dollinger, G. (2008)
757 Application of Raman spectroscopy to quantify trace water concentrations in glasses and garnets.
758 American Mineralogist, 93, 1550-1557.
759
760 Thomas S.-M., Koch-Müller M., Reichart P., Rhede D., Thomas R., Wirth R. and Matsyuk S.
761 (2009) IR calibrations for water determination in olivine, r-GeO2 and SiO2 polymorphs. Phys
762 Chem Mineral, 36, 489 - 509.
763
764 Van Orman, J.A. and Crispin, K.L. (2010) Diffusion in Oxides. Reviews in Mineralogy and
765 Geochemistry, 72, 775-825.
766

767   Vlassopoulos, D., Rossman, G.R., and Haggerty, S.E. (1993) Coupled substitution of H and minor
768   elements in rutile and the implications of high OH contents in Nb- and Cr-rich rutile from the upper
769   mantle. American Mineralogist, 78, 1181-1191.

771   Wahlbeck, P.B. and Gilles, P.W. (1966) Reinvestigation of the phase diagram for the system
772   titanium-oxygen. Journal of the American Ceramic Society, 49, 180-183.

774   Zack, T., Kronz, A., Foley, S.F. and Rivers, T. (2002) Trace element abundances in rutiles from
775   eclogites and associated garnet mica schists. Chemical Geology, 184, 97-122.

777   Zaleska, A. (2008) Doped-TiO_2: A Review. Recent Patents on Engineering, 2, 157-164.

779   Zheng, Y.-F. (2009) Fluid regime in continental subduction zones: petrological insights from
780   ultrahigh-pressure rocks. Journal of the Geological Society, London, 166, 2009, 763–782.

782   **Figure captions**

784   **Figure 1** Scanning electron microscope image of a reacted synthetic rutile (run RT38). The crystal
785   plate for FTIR was cut from the centre of the cube parallel (110) and polished on both faces. The
786   size of the crystal is ~1 mm^3 with an edge length of 1 mm.

788   **Figure 2** (a,b) Transmitted light images of experimental products after 14 days run time. (a) Pure
789   rutile, run RT30a; (b) Fe-doped rutile, run RT30b. Yellow squares indicate the position of the FTIR
790   analyses; numbers are calculated H_2O equivalent in ppm. (c,d) Polarized FTIR absorbance spectra,
791   run RT30a, reacted and untreated material (d is enlarged part of c). There is no absorbance for **E** ||
792   *c*. (e) Raman spectrum, sample RT30a. The signal of the unreacted sample is very weak **E** $\perp$ *c*, but
793   at the same wave number as the large signal from the reacted sample. There is no signal for **E** || *c*
794   *(upper spectrum for reacted sample, not labeled). t = thickness of sample.*

796   **Figure 3** UV-VIS polarized spectra of (a) untreated pure rutile, run RT30a; (b) reacted pure rutile,
797   run RT30a; (c) untreated Fe-doped rutile, run RT30b. The spectra of reacted rutile (run RT30b) are
798   nearly identical with those of RT30a in (b) and not shown. For discussion see text. The different
799   positions of the high-energy absorption edge are due to different thickness, t, of the samples.

801   **Figure 4** Transmitted light images of reacted (a) Nb-doped rutile (run RT36; 14 days) and (b) Cr-
802   doped rutile, run RT38 (14 days). Yellow squares indicate the position of the FTIR analyses;
803   numbers are the calculated H_2O equivalent in ppm.

805   **Figure 5** Polarized UV-VIS spectra of Cr-doped rutile, run RT38 (a) untreated and (b) reacted and
806   unpolarized UV-VIS spectra of the two color varieties of reacted V-doped rutile RT37 (c); see text
807   for discussion.

809   **Figure 6** (**a**) Microphotograph of hydrated Nb-doped rutile (run product RT40) before the heating
810   experiment. The measuring cycle for the heating experiment is Z-R1-R2-Z'; the direction of *c* is
811   horizontal. (**b**) Results of the heating experiment, H_2O equivalent versus time for the different
812   heating steps; the distances between the heating steps correspond to the time of heating and to the
813   acquisition of the background. Variability of the H_2O contents between Z-R1-R2-Z' and in-between
814   the acquisition cycles is significant but not systematic up to 450°C. The average (av.) of the four
815   measurements per cycle starts to decrease above 350°C. No OH signal was seen in the IR spectra at
816   600 °C and 650 °C.

817

23

818   **Figure 7** H_2O contents (measured by FTIR spectroscopy) and trace element composition (LA-ICP-
819   MS; Lucassen et al. 2010) of a large natural rutile with titanite overgrowth. (a) Scanning electron
820   microscope image of the right hand side of the profile in (b), polished sample surface with pits from
821   LA-ICP-MS analyses and the position of FTIR measurements with H_2O content in ppm. (b) Profile
822   through the rutile crystal with Fe, Nb, and Zr and $H_2O_{(IR)}$ contents; neighbored pairs of LA and
823   FTIR spectroscopy spots are connected by thin lines. (c) Comparison of measured $H_2O_{(IR)}$ and
824    $H_2O_{(Fe)}$ contents, calculated from measured Fe corrected for Nb contents (see text). (d) Correlation
825   between $H_2O_{(Fe)}$ and $H_2O_{(IR)}$; although there is considerable scatter, the fact that the two values are
826   from a completely different approach underlines the positive correlation.
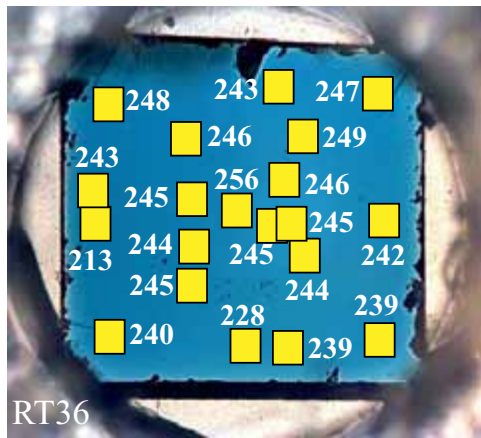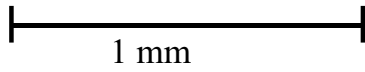827
828

Figure 1

a.

b.

(c)

(d)

(e)
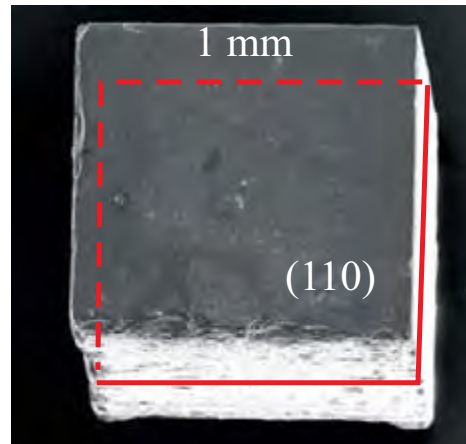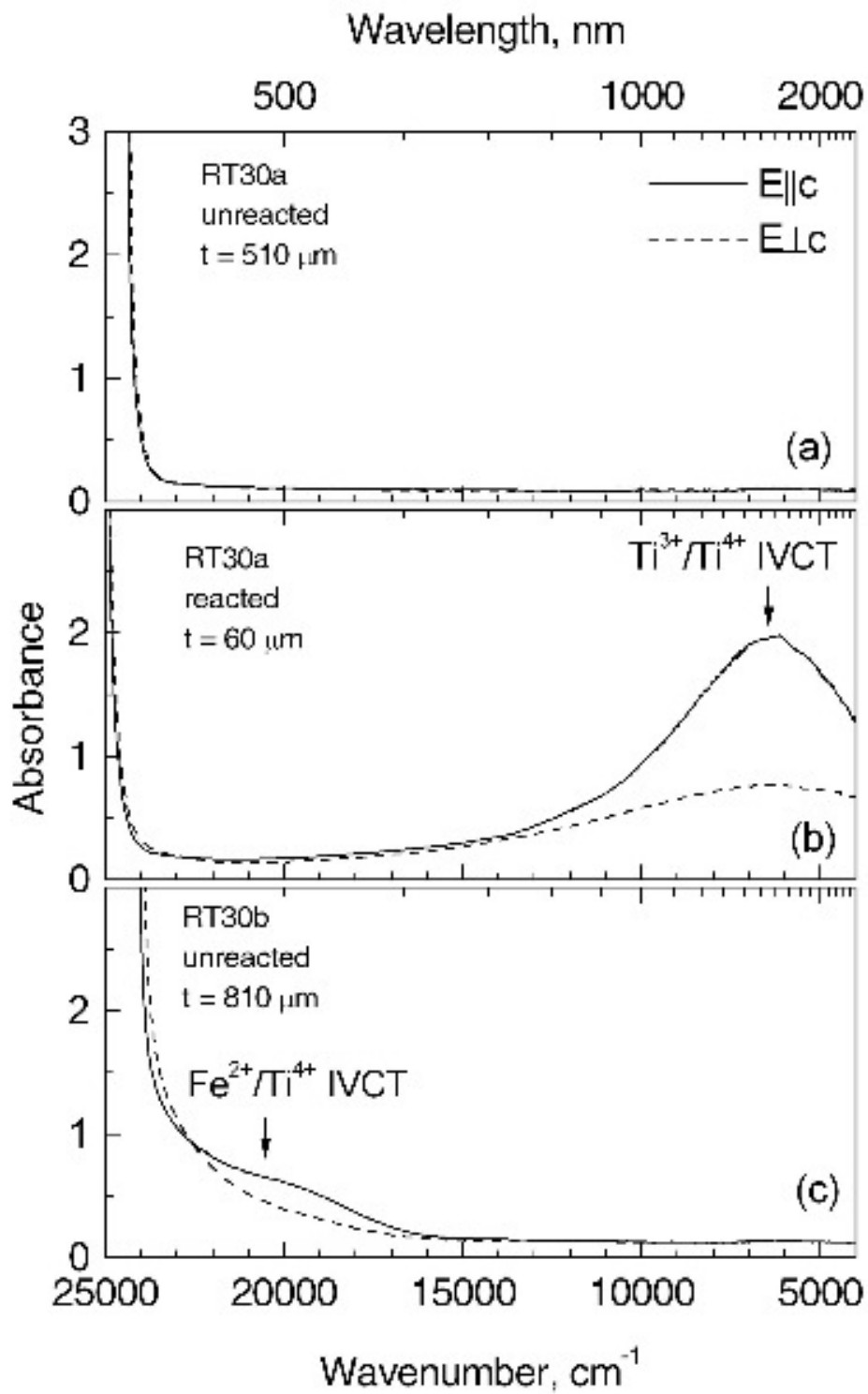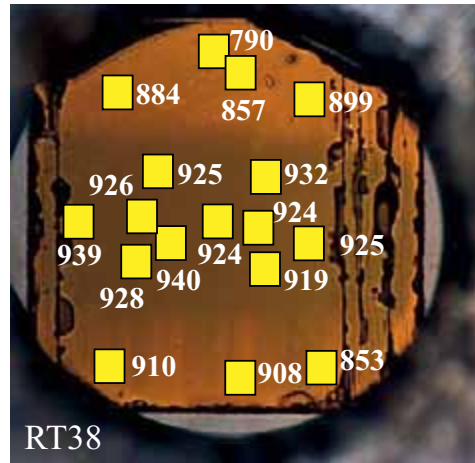
Figure 2
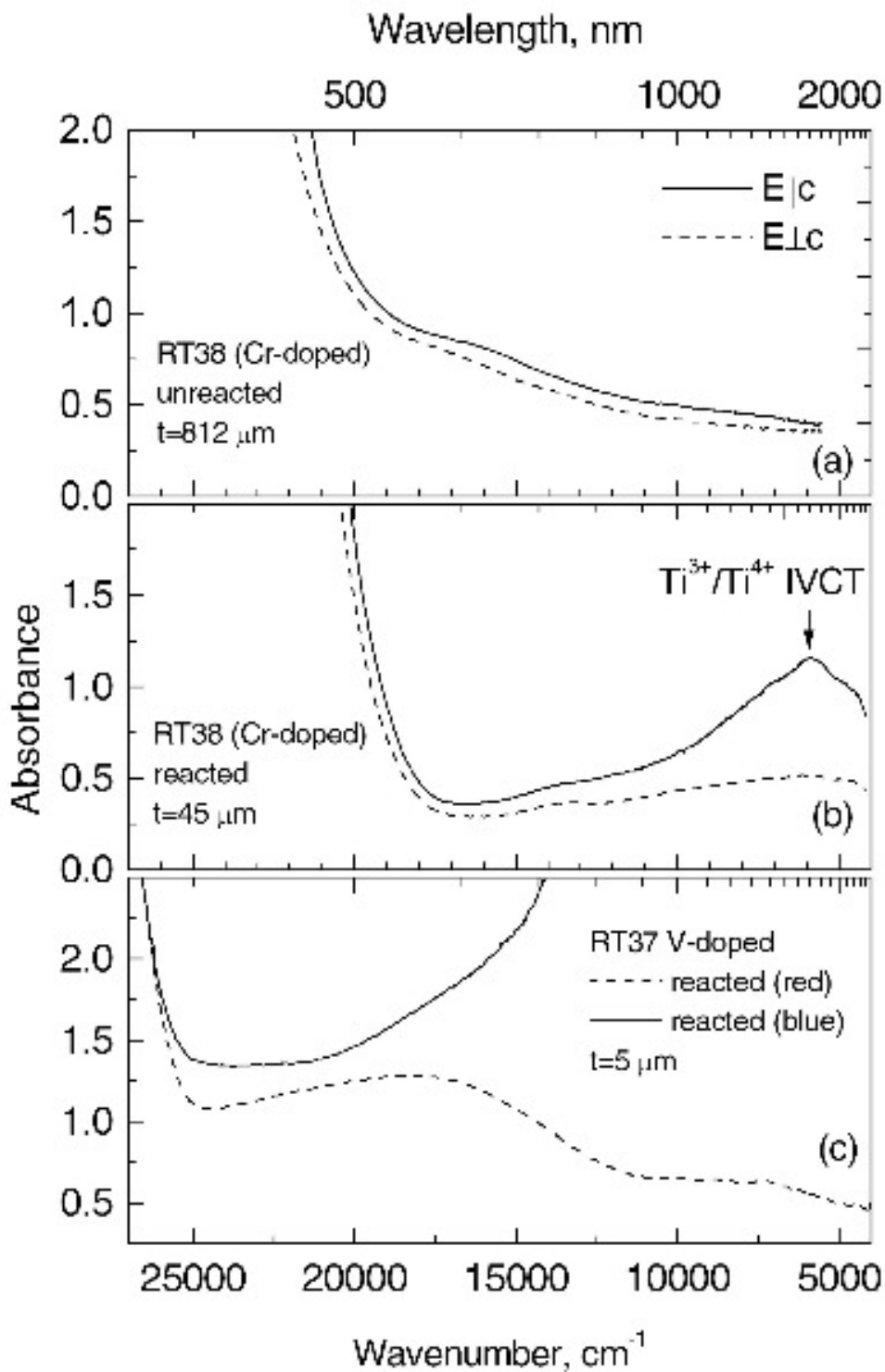
Figure 3
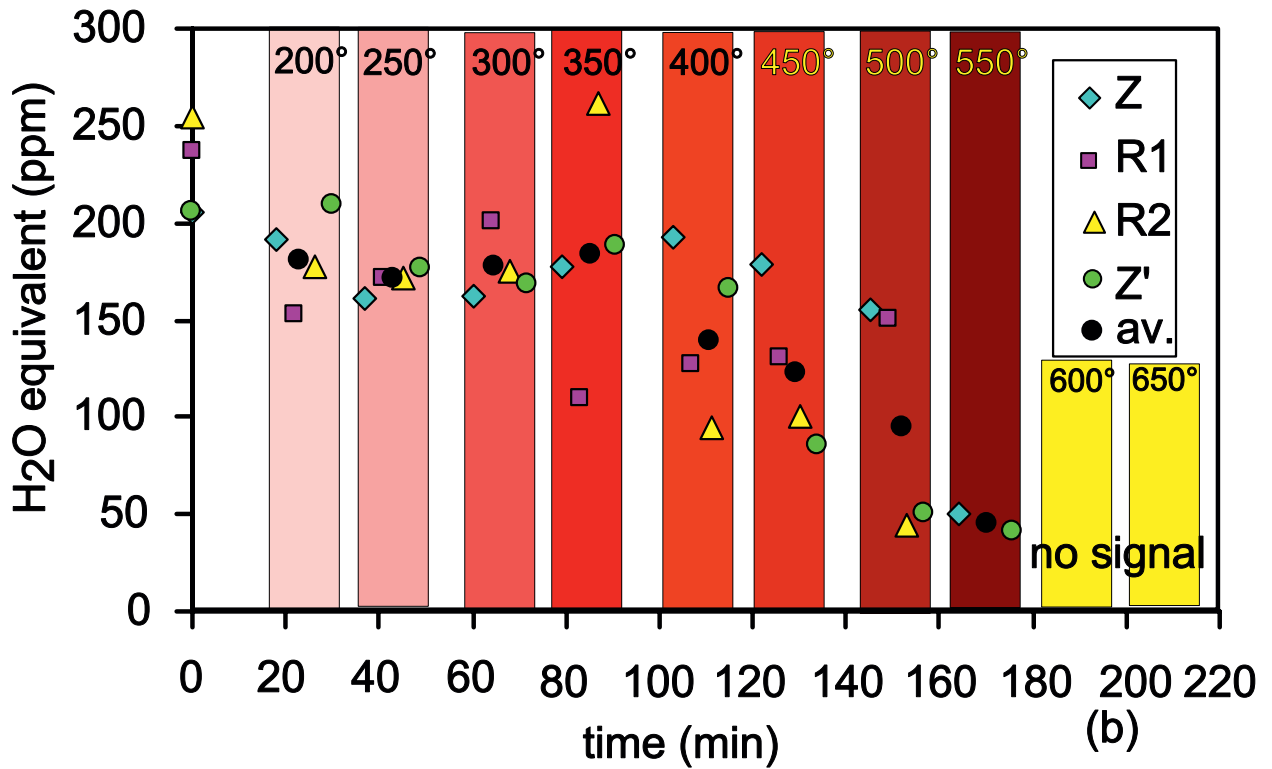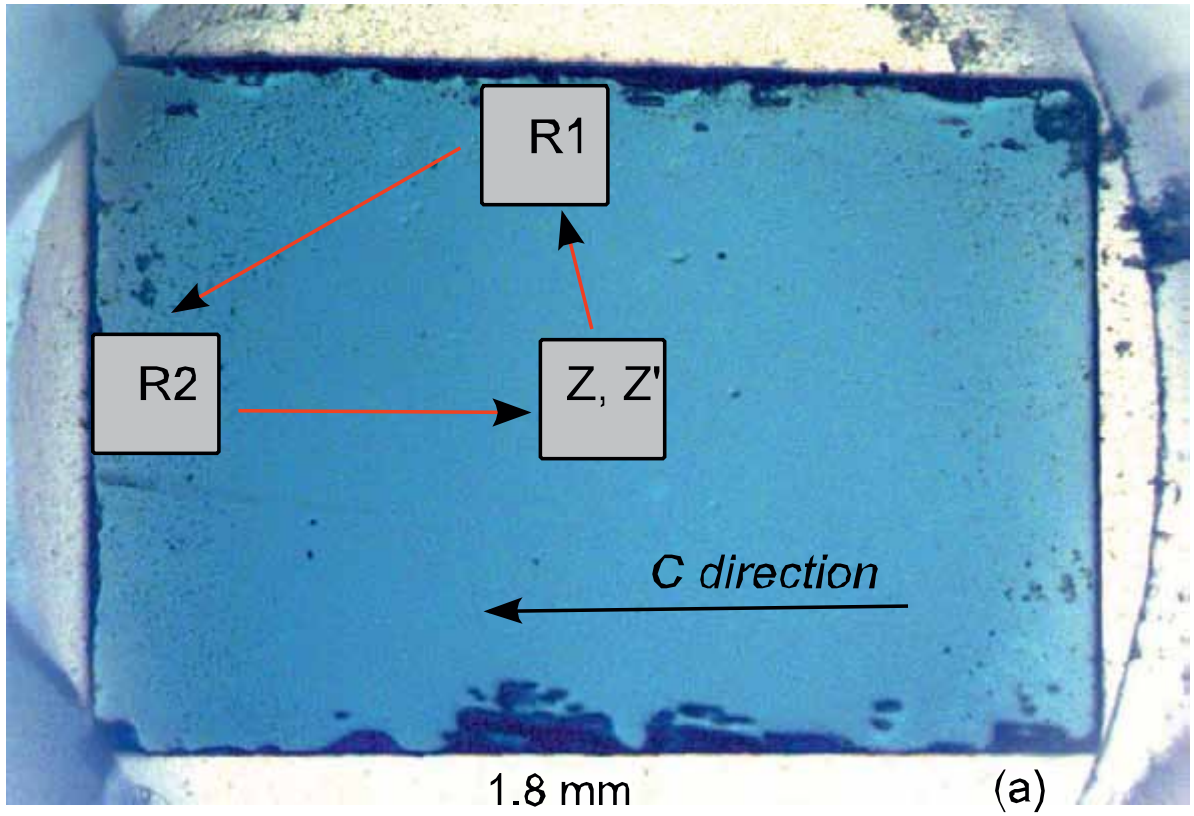
Figure 4

Figure 5
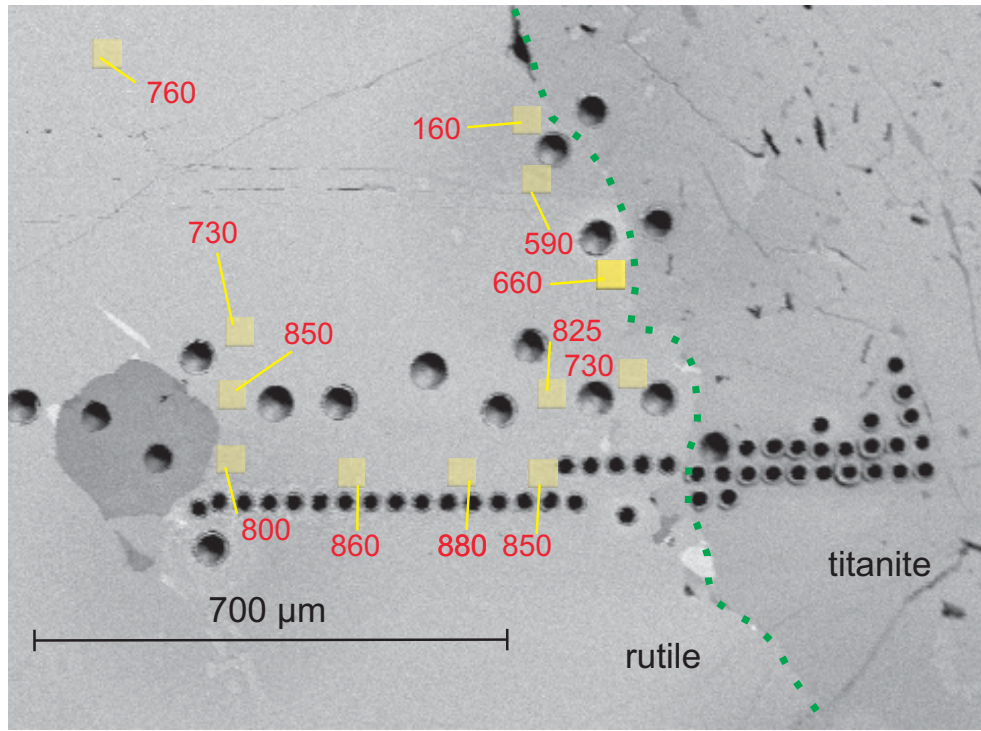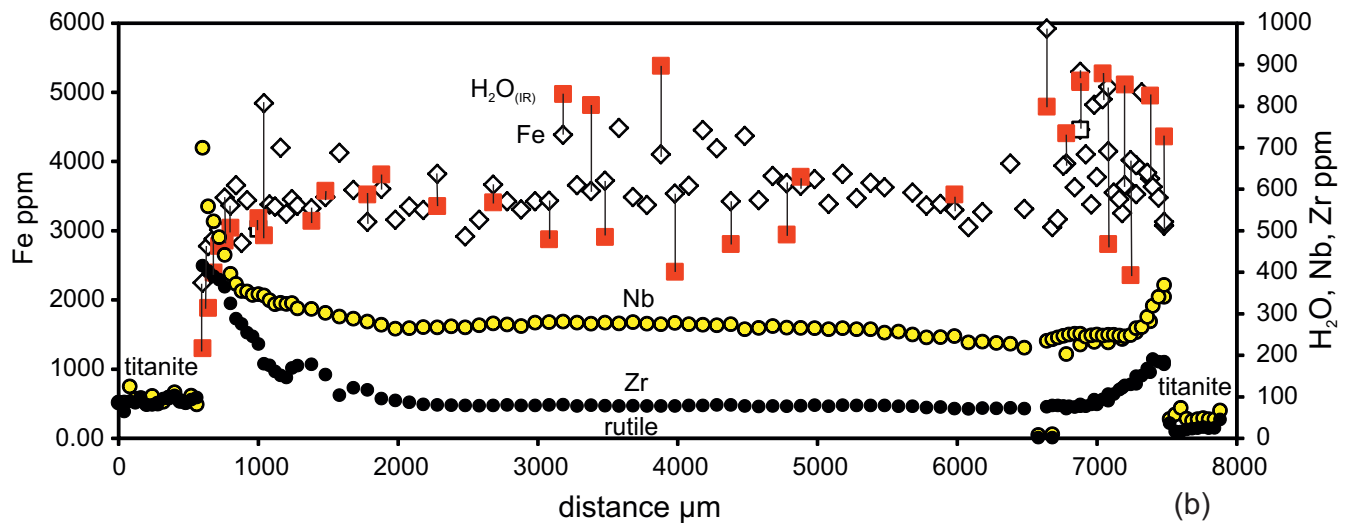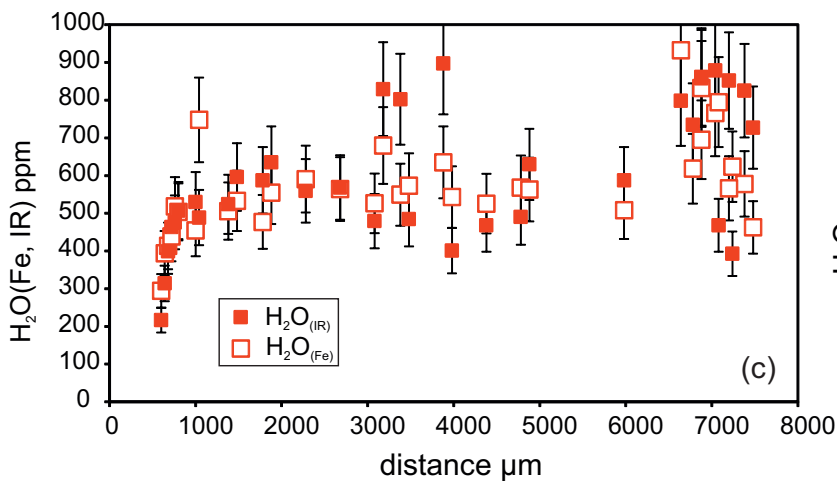
Figure 6

$H_2O_{(IR)}$ in ppm

(a)

(b)

(c)

(d)

Figure 7
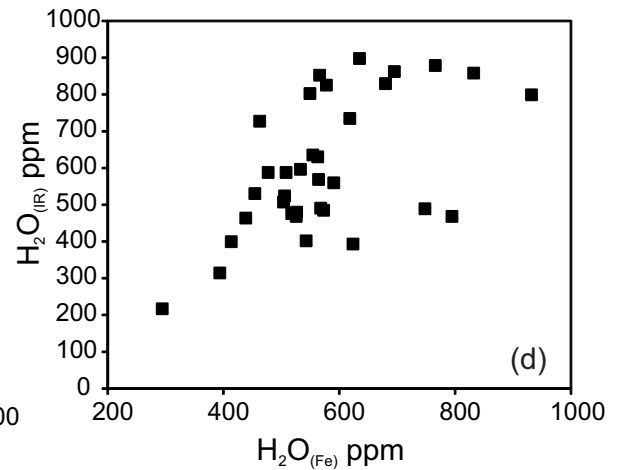
Table 1 Results of the experiments; for errors on thickness and ppm H_2O see text

run#	RT30a	RT30b	RT34	RT44	RT47	RT48	RT40	RT36	RT38	RT37	RT75
rutile type	pure			traces of Fe			500 ppm Nb		2000 ppm Cr	2000 ppm V	
duration	14 days	14 days	48 h	8 h	1 h	~25 min*	14 days	14 days	14 days	14 days	7 days
thickness µm	66	66	62	67	65	53	60	59	70	5	10
number of data	11	13	21	24	18	25	18	20	17		
H_2O ppm	332±35	344±33	298±23	360±26	271±22	270±19	229±19	242±19	901±77	-	-
H_2O range	330 - 335	324-358	256-336	290-394	258-284	237-313	203-277	215 - 256	790-940		
~n H^+/cm^3 rutile**	$9.44 \cdot 10^{19}$	$9.8 \cdot 10^{19}$	$8.49 \cdot 10^{19}$	$1.04 \cdot 10^{20}$	$7.71 \cdot 10^{19}$	$7.76 \cdot 10^{19}$	$6.88 \cdot 10^{19}$		$2.57 \cdot 10^{20}$	-	-
~n atoms trace element/cm^3 rutile	-	-	-	-	-	-	$1.4 \cdot 10^{19}$		$9.8 \cdot 10^{19}$	$1.0 \cdot 10^{20}$	
			Ti				Nb		Cr	V	
Shannon radii for vi coordination Å			3^+ 0.67 4^+ 0.605				3^+ 0.72 4^+ 0.68 5^+ 0.64		2^+ 0.73 3^+ 0.615 4^+ 0.55 5^+ 0.49 6^+ 0.44	3^+ 0.64 4^+ 0.58 5^+ 0.54	

* heating – quenching experiment; (-) below detection limit.** average value for RT30a,b,34,44,47,48 is $8.9 \cdot 10^{19}$ atoms H equivalent to Ti cm^{-3}

Table 2 Trace element (LA-ICP-MS) and water contents, measured (H_2O_{IR}) and (H_2O_{Fe}) calculated from Fe and corrected for Nb contents (see text) along a profile in a natural rutile crystal (see Fig 7b).

distance (μm)	Fe (ppm)	Nb (ppm)	Zr (ppm)	$H_2O_{(IR)}$* (ppm)	$H_2O_{(Fe)}$ (ppm)
600	2250	700	420	220	290
640	2780	560	400	310	390
680	2880	520	390	400	410
720	3010	480	380	460	440
760	3480	440	370	480	520
800	3360	400	330	510	500
1000	3030	350	230	530	450
1040	4840	340	180	490	750
1380	3320	310	180	520	510
1480	3490	302	150	600	530
1780	3130	280	120	590	480
1880	3600	270	95	640	560
2280	3820	270	80	560	590
2680	3670	280	79	570	560
3080	3430	280	80	480	530
3180	4380	280	81	830	680
3380	3570	280	79	800	550
3480	3720	280	78	490	570
3880	4100	280	78	900	640
3980	3530	280	78	400	540
4380	3420	280	81	470	530
4780	3680	270	77	490	570
4880	3650	270	79	630	560
5980	3300	250	71	590	510
6640	5920	240	76	800	930
6780	3970	200	72	730	460
6880	5300	230	82	860	830
6880	4460	250	77	860	700
7040	4900	250	94	880	770
7080	5080	250	91	470	800
7200	3660	250	130	850	570
7240	4020	250	130	390	620
7380	3750	280	160	830	580
7480	3070	340	180	730	460

* for errors see text